



Deposited via The University of Sheffield.

White Rose Research Online URL for this paper:

<https://eprints.whiterose.ac.uk/id/eprint/127690/>

Version: Published Version

---

**Article:**

Keen, J.A., Lane, D., Kesaria, M. et al. (2018) InAs/InAsSb type-II strained-layer superlattices for mid-infrared LEDs. *Journal of Physics D: Applied Physics*, 51 (7). 075103. ISSN: 0022-3727

<https://doi.org/10.1088/1361-6463/aaa60e>

---

**Reuse**

This article is distributed under the terms of the Creative Commons Attribution (CC BY) licence. This licence allows you to distribute, remix, tweak, and build upon the work, even commercially, as long as you credit the authors for the original work. More information and the full terms of the licence here:

<https://creativecommons.org/licenses/>

**Takedown**

If you consider content in White Rose Research Online to be in breach of UK law, please notify us by emailing [eprints@whiterose.ac.uk](mailto:eprints@whiterose.ac.uk) including the URL of the record and the reason for the withdrawal request.

PAPER • OPEN ACCESS

## InAs/InAsSb type-II strained-layer superlattices for mid-infrared LEDs

To cite this article: J A Keen *et al* 2018 *J. Phys. D: Appl. Phys.* **51** 075103

View the [article online](#) for updates and enhancements.



### LIVE WEBINAR

NanoRaman: Correlated Tip-Enhanced Optical Spectroscopy and Scanning Probe Microscopy

Thursday 8 March 15.00 GMT

REGISTER NOW!

[physicsworld.com](http://physicsworld.com)

# InAs/InAsSb type-II strained-layer superlattices for mid-infrared LEDs

J A Keen<sup>1</sup>, D Lane<sup>1</sup>, M Kesaria<sup>2</sup>, A R J Marshall<sup>1</sup> and A Krier<sup>1</sup>

<sup>1</sup> Physics Department, Lancaster University, Lancaster, LA1 4YB, United Kingdom

<sup>2</sup> Electronic and Electrical Engineering Department, University of Sheffield, Sheffield, S3 7HQ, United Kingdom

E-mail: [j.keen@lancaster.ac.uk](mailto:j.keen@lancaster.ac.uk)

Received 8 November 2017, revised 3 January 2018

Accepted for publication 8 January 2018

Published 30 January 2018



## Abstract

InAs/InAsSb type-II strained-layer superlattice (SLS) and multiple quantum well (MQW) structures have been studied for their suitability in the active region of mid-infrared LEDs operating at room temperature. A series of InAs/InAs<sub>1-x</sub>Sb<sub>x</sub> superlattices with low antimony content ( $x = 3.8\text{--}13.5\%$ ) were grown by MBE on InAs substrates and characterised using x-ray diffraction and photoluminescence (PL). The 4 K PL spectra of these samples exhibit the expected peak shift to longer wavelength and a reduction in intensity as the Sb content is increased. Band structure simulations highlight the effects of changing the antimony content and the layer thicknesses, to tailor the overlap of the electron and hole wavefunctions and maximise the radiative recombination rate. Analysis of the temperature dependence of the PL emission spectra enabled the extraction of quenching energies that demonstrate some suppression of Auger recombination in both the MQW and SLS structures. The MQW samples exhibit a changeover in the dominant radiative recombination process above  $\sim 100$  K associated with thermal emission of holes into the InAs barriers; this behaviour was not observed in the SLS samples. These SLS structures have the potential for use as the active region in room temperature mid-infrared LEDs.

Keywords: InAs/InAsSb, superlattice, type-II, mid-infrared, LED

(Some figures may appear in colour only in the online journal)

## Introduction

Detecting and monitoring the presence of gases such as methane (CH<sub>4</sub>), carbon monoxide (CO) and carbon dioxide (CO<sub>2</sub>), which have unique absorption spectra within the mid-infrared (MIR) spectral range, is desirable for numerous applications in different industries particularly for environmental monitoring because of their harmful effects on the earth's atmosphere [1]. Light emitting diodes (LEDs) are a promising alternative to laser-based devices for the detection of these gases due to their favourable operating properties including:

lower power consumption, easier implementation, lower complexity and lower cost [2]. However, the efficiency of MIR LEDs at room temperature is significantly lower than those operating at visible and near-infrared wavelengths because of detrimental non-radiative Auger and SRH recombination processes. In this respect, type-II InAs/InAsSb superlattice structures continue to attract research interest because of the ability to tailor the band structure to target specific emission wavelengths as well as the potential to adjust electron–hole separation to reduce non-radiative Auger recombination and maximise the rate of radiative recombination [3, 4]. This makes them excellent candidates for use in the active region of MIR LEDs. The majority of research to date has focused on the study of InAs/InAsSb structures grown lattice-matched and therefore unstrained onto GaSb substrates [5, 6] comprising



Original content from this work may be used under the terms of the [Creative Commons Attribution 3.0 licence](https://creativecommons.org/licenses/by/3.0/). Any further distribution of this work must maintain attribution to the author(s) and the title of the work, journal citation and DOI.

numerous thick InAsSb layers of high antimony content, as required for the development of MIR photodetectors [7–10]. These superlattices have also been quite successful as the active regions in lasers [11–13]. But, there have been fewer reports of MIR LEDs using these structures [14–16]. In this work we report on InAs/InAsSb strained-layer superlattices (SLS) grown on InAs substrates. There are some advantages of such structures: firstly, a smaller bandgap can be achieved as the strain makes the structure more type II; secondly, the strain breaks the degeneracy of the heavy hole and light hole bands, which can help to reduce Auger recombination which is particularly detrimental to LED performance at higher temperatures.

## Experimental procedures

A series of four InAs/InAs<sub>1-x</sub>Sb<sub>x</sub> SLS structures were grown, comprised of 50 periods of 14nm InAs and 14nm InAsSb with antimony content  $x = 3.8\text{--}13.5\%$ , on n-InAs(100) substrates in a VG-V80H MBE system. Two multiple quantum well (MQW) InAs/InAsSb structures (40nm InAs barrier, 10nm InAsSb QW) containing  $x_{\text{Sb}} = 3.7, 4.3\%$  were also grown based on our earlier work [17]. Valved cracker cells were used to provide As and Sb fluxes and a thermal effusion K-cell was used to provide the In flux. During the growth surface reconstructions were monitored by *in situ* reflection high energy electron diffraction (RHEED). Substrate temperature was measured using an infrared pyrometer and back-calibrated by monitoring surface reconstructions. The growth rates were calibrated by monitoring RHEED spot intensity oscillation using a photomultiplier tube. The substrate is first outgassed in the preparation chamber and oxide desorption is carried out in the growth chamber by gradually heating up to 520 °C under As flux until the weak  $\times 3$  RHEED pattern transforms to the  $\times 2$  pattern. The substrate temperature is lowered to 480 °C to grow an InAs buffer layer of thickness 600 nm and then further reduced to 450 °C to carry out growth of the InAs/InAsSb SLS and MQW. To obtain abrupt interfaces between InAsSb and InAs, As–Sb exchange is done by exposing the InAs surface to Sb flux for 10 s prior to InAsSb QW and SLS layer growth and before InAs barrier growth the InAsSb surface is exposed to As flux for 20 s. Antimony composition of the InAsSb layers was varied by controlling the temperature of the Sb cell, starting at 550 °C to achieve Sb = 3.8% and increased up to 580 °C to achieve Sb = 13.5%. Details are of the samples are given in table 1.

All the samples were characterised using high resolution x-ray diffraction (XRD) using a Bede QC 200 system to obtain  $\omega - 2\theta$  scans. Bede Mercury RADS simulation software based on dynamical scattering theory of XRD was used to determine the layer thicknesses and Sb content. Photoluminescence of the structures was excited using a 785 nm laser focused onto the sample which was held inside an Oxford Instruments continuous flow cryostat, capable of maintaining the sample at a fixed temperature in the range 4–300 K. The spot size was 1 mm (diameter) corresponding to an excitation of approximately  $2.5 \text{ Wcm}^{-2}$  at the sample surface. The photoluminescence (PL) emission was analysed using a Bruker Vertex 70

**Table 1.** A summary of the structure details of the different samples under investigation. Thickness and composition values were measured using high resolution XRD.

Sample	Structure	InAs barrier (nm)	InAsSb QW (nm)	No. of periods	Sb content, $x$ (%)
1	MQW	40.0	10.0	10	3.7
2	MQW	40.0	10.0	10	4.3
3	SLS	14.0	14.0	50	3.8
4	SLS	14.0	14.0	50	6.2
5	SLS	14.0	14.0	50	9.5
6	SLS	14.0	14.0	50	13.5

Fourier transform infrared (FTIR) spectrometer in step scan mode. The radiation was detected using a 77 K InSb photodetector and lock-in amplifier.

## Results

### InAs/InAsSb multiple quantum wells (MQW)

The  $\omega - 2\theta$  XRD spectra obtained from the (004) x-ray rocking curves of the two MQW samples are shown in figure 1. These were peak matched with theoretical scan data simulated by RADS Mercury software. The InAs barrier and InAsSb well thickness were obtained as 40nm and 10nm respectively and the Sb content was determined to be 3.7% and 4.3% in Sample 1 and Sample 2 respectively, in close agreement with the target design. The strong Pendellosung fringes are evidence of good structural layer quality and sharp growth interfaces.

The corresponding FTIR PL spectra obtained from the MQW samples obtained at temperatures in the range 4–300 K are shown in figure 2. The PL spectra are comprised of double peaks situated at wavelengths relatively close to one another which were separated by Gaussian deconvolution. At 4 K the energy separation between the two deconvoluted peaks is small, at around 3.7 meV and 5.4 meV for Sample 1 and (more clearly visible) in Sample 2 respectively which is consistent with exciton recombination in the quantum well and which is as expected approximately 4 times the exciton binding energy in the bulk semiconductor [18, 19] (assuming an exciton binding energy of 1.3 meV in bulk InAs, and is proposed to be discussed in detail in a further publication). The PL decreases in intensity as temperature is increased. The two most important non-radiative processes are SRH and Auger recombination. The rate at which SRH recombination occurs is relatively insensitive to temperature [20]. However, Auger recombination is known to be temperature dependent and follows the general relation

$$R_{\text{Auger}} \propto \exp\left(-\frac{E_a}{k_B T}\right) T^3 \quad (1)$$

where  $E_a$  is the activation energy for the corresponding Auger process and the exponential term dominates [21]. The specific Auger processes each have their own activation energies, where the CHCC and CHSH processes have activation energies given by [22]

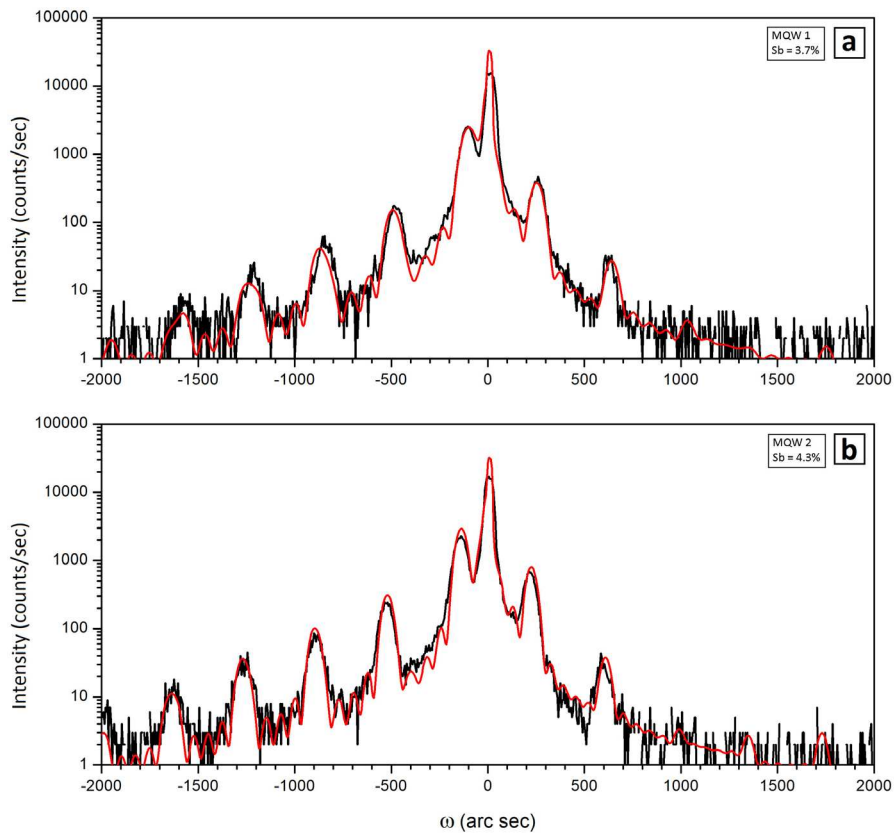


**Figure 1.** XRD scan comparison with simulated data for (a) Sample 1 (MQW, Sb = 3.7%) and (b) Sample 2 (MQW, Sb = 4.3%). Black line—XRD data, red line—simulation.

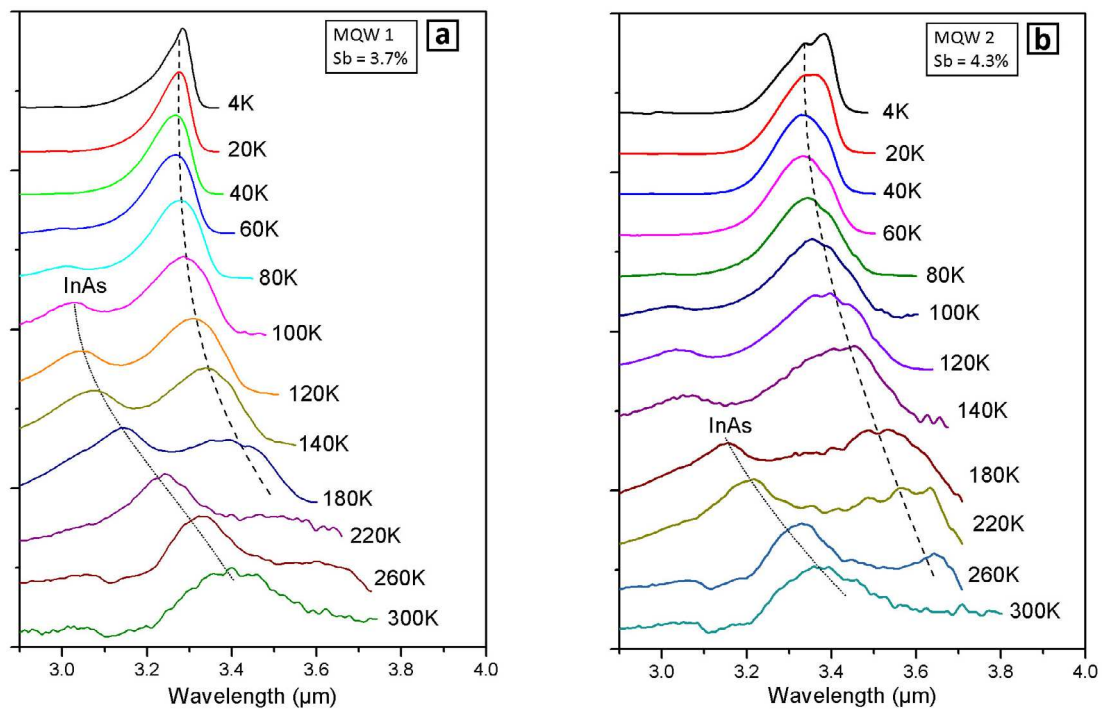


**Figure 2.** The temperature dependence of PL obtained from the two MQW samples: (a) Sample 1 containing 3.7% Sb in the MQW and (b) Sample 2 containing 4.3% Sb in the MQW. The lines are a guide to the eye, where the dotted line follows the peak from the  $e_1-hh_1$  transition in the type-II structure, and the solid line follows the peak from recombination in the InAs layers.

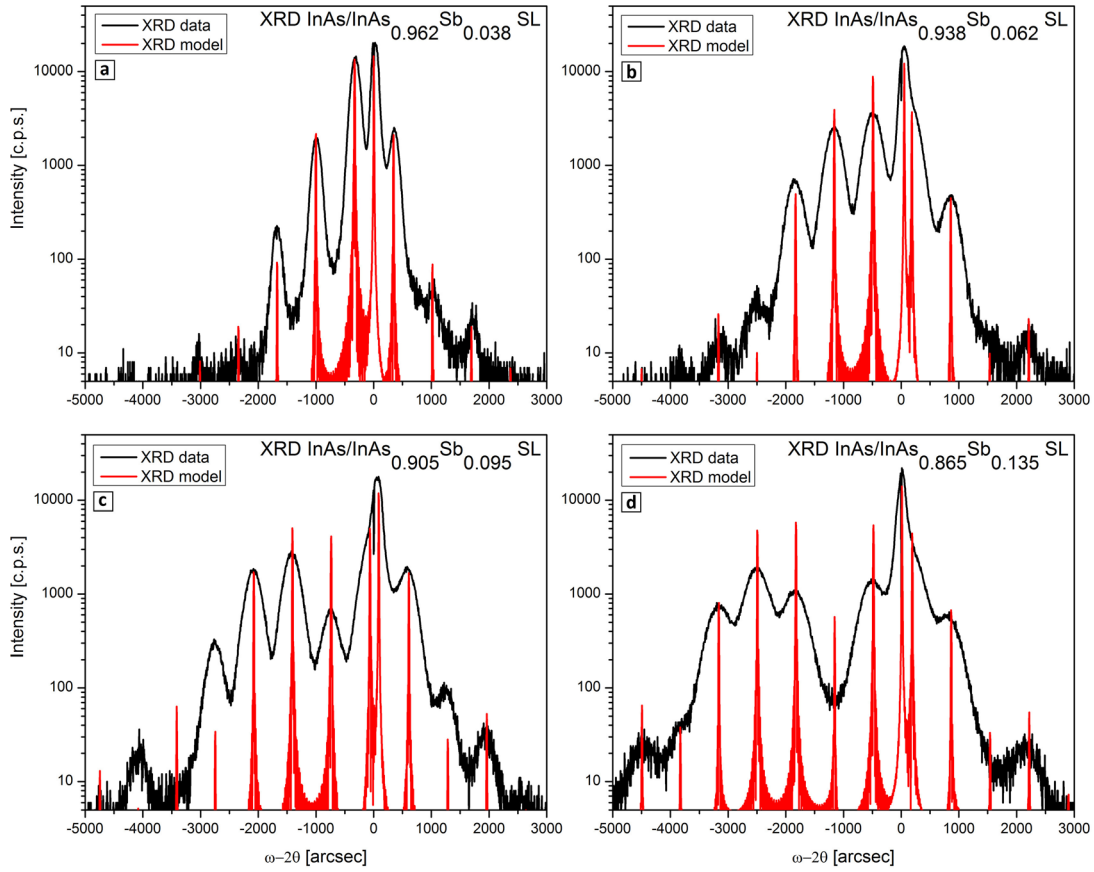


**Figure 3.** XRD scans and comparison with simulated data for the SLS samples; (a) Sample 3 (Sb = 3.8%), (b) Sample 4 (Sb = 6.2%), (c) Sample 5 (Sb = 9.5%) and (d) Sample 6 (Sb = 13.5%). Black lines—XRD data, red lines—simulation.

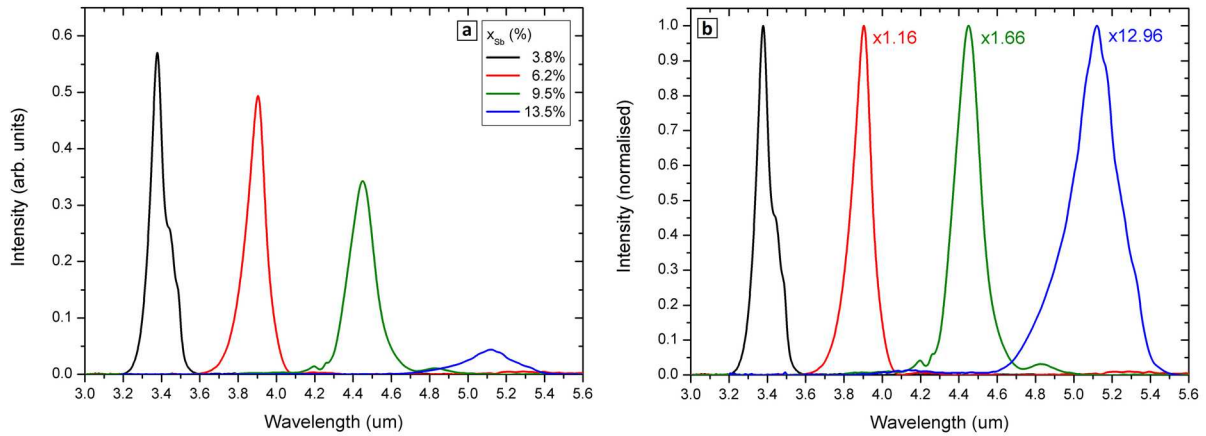


**Figure 4.** PL spectra obtained from each of the SLS samples (a) 4 K PL spectra of InAs/InAs<sub>1-x</sub>Sb<sub>x</sub> SLS structures with increasing Sb content; (b) normalised 4 K PL spectra of those shown in (a) highlighting the decrease in intensity with increasing Sb.

$$E_a^{\text{CHCC}} = \frac{m_e^* E_g}{m_e^* + m_{hh}^*} \quad (2)$$

$$E_a^{\text{CHSH}} = \frac{m_{SO}^*}{m_e^* + 2m_{hh}^* - m_{SO}^*} (E_g - \Delta_0) \quad (3)$$

where  $E_g$  is the bandgap energy,  $\Delta_0$  is the spin orbit splitting energy, and  $m_e^*$ ,  $m_{hh}^*$ ,  $m_{SO}^*$  are the effective masses of the

electrons, holes in the heavy hole band and holes in the split off band respectively. It is possible to determine the dominant Auger process using,

$$\frac{(E_T - \Delta_0)/E_T}{m_e^*/m_{SO}^*} > 1 \quad (4)$$

such that the CHCC process is dominant when this condition is satisfied. ( $E_T$  is the transition energy corresponding to  $e_1 - hh_1$  recombination).

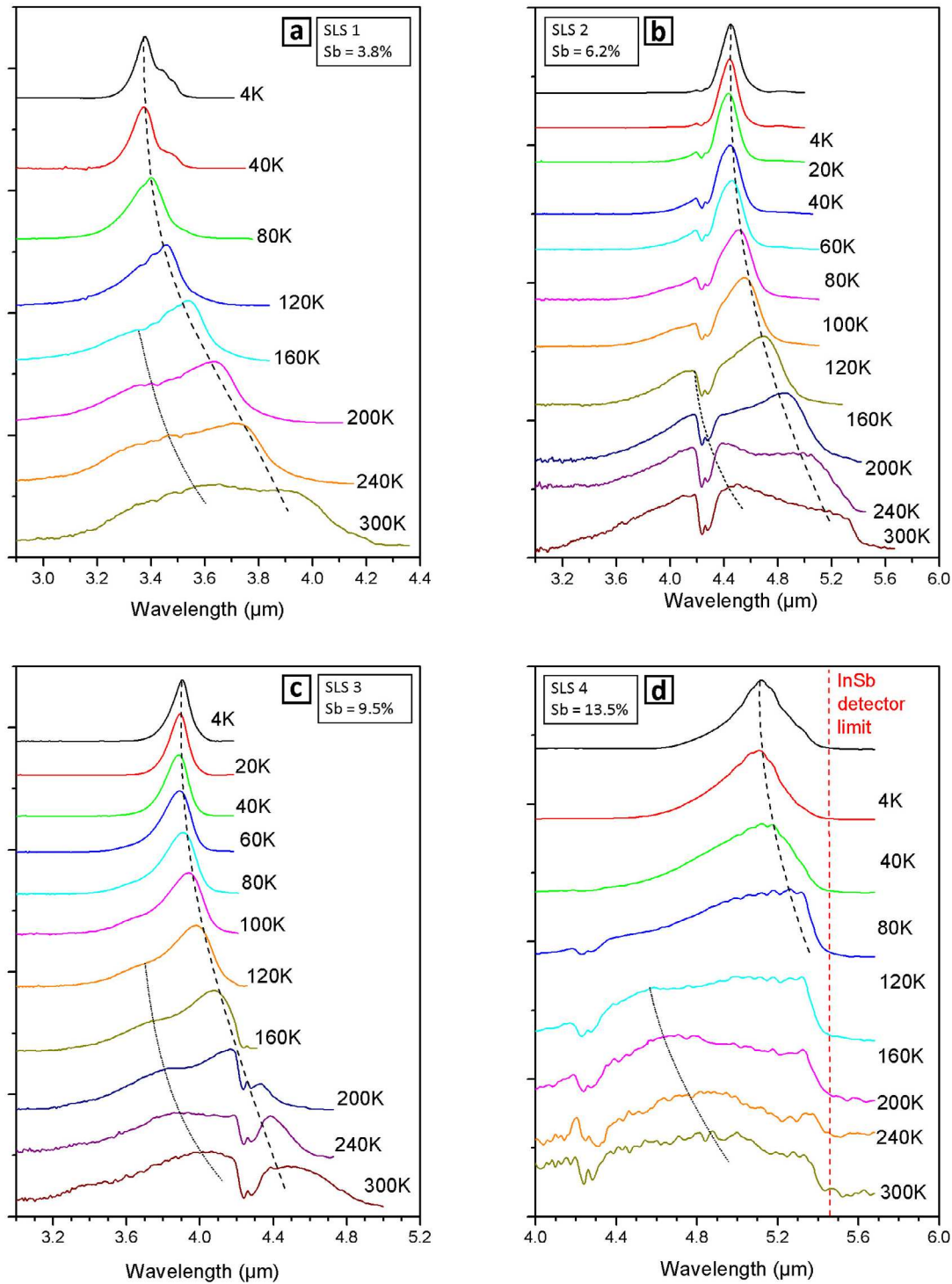


**Figure 5.** Normalised PL spectra for all of the SLS samples at increasing temperatures. As a guide to the eye the dashed line indicates the  $e_1 - hh_1$  transition, the dotted line at shorter wavelength indicates the  $e_1 - hh_2$  transition.

The evolution of the  $e_1 - hh_1$  main peak in the PL spectra of the MQW with increasing temperature shows the characteristic red-shift due to bandgap narrowing and follows closely the well-known Varshni law [23]. In both samples, above about 80 K, PL emission begins to appear from the InAs barriers originating from thermal emission of confined holes escaping from the MQW. This process continues up to room temperature where it dominates to the extent that there is no longer any observable PL emission from the MQW. This is

in contrast to the behaviour in the SLS samples considered below.

#### *InAs/InAsSb strained-layer superlattices (SLS)*

The four SLS samples were also characterised using high resolution XRD and the (004) x-ray rocking curves are shown in figure 3 together with the corresponding simulations. These samples contain 50 periods of InAs/InAsSb (compared with

ten in the MQW samples) with much thinner InAs barriers—see table 1 for details. The measured fringes are broader compared to the simulation, but the Pendellosung fringes are clearly visible, which indicates good layer quality and very low Sb segregation into the InAs wells. In each case the simulation gives the corresponding Sb content and the thickness of the InAsSb QW and InAs barrier thickness as 14.0 nm. The strain increases with Sb content and calculations using the Matthews Blakeslee model [24, 25] revealed that the critical thickness is just exceeded for Sample 6 containing the highest Sb content, which means that sample this sample may contain some dislocations. This is consistent with the reduced structural quality evident in the XRD scan where the peaks are less well defined compared to those in the other samples with lower Sb content.

The 4 K photoluminescence spectra of the InAs/InAs<sub>1-x</sub>Sb<sub>x</sub> SLS structures in figure 4 show behaviour in good agreement with previously reported PL results on similar structures [26]. It is evident that as Sb content of the InAs<sub>1-x</sub>Sb<sub>x</sub> layers increases the PL emission shifts to longer wavelengths, the intensity decreases, and the peak broadens, which is consistent with spatially indirect transitions in type-II QW [17]. As shown in the normalised spectra of figure 5(b) the peak intensity decreases by ~13 times as Sb content is increased from 3.8% to 13.5% and the full width half maximum increases from ~97 nm to ~270 nm.

The temperature dependent PL spectra from each of the InAs/InAs<sub>1-x</sub>Sb<sub>x</sub> SLS are shown together in figure 5. The PL peak corresponding to the  $e_1 - hh_1$  ground state transition is identifiable in all cases from 4 K up to 300 K. All samples exhibit thermal broadening of ~1.1–1.7  $k_B T$ . Unlike the MQW samples, the holes remain strongly confined and the PL spectra of the SLS samples do not display a peak corresponding to the InAs barrier transition as temperature is increased. However, an additional peak is observed in all of the SLS samples. This peak is of higher energy than the  $e_1 - hh_1$  peak and is of a different energy for each sample and becomes visible above ~60 K in each case. The energy separation between these peaks ranges from 15 meV to 26 meV, consistent with  $e_1 - hh_2$  transitions to the next confined hole state in the quantum well (—dotted lines in figure 5). The peak energy is dependent on the composition and is consistent with the finite square well approximation for energy levels in the type-II quantum wells. The PL linewidth of the SLS is very similar to that of the MQW samples.

## Discussion

The band structures of the InAs/InAsSb type-II structures were calculated using Nextnano [26] software, assuming rectangular quantum wells and periodic boundary conditions. The strain in the structure is included within the program according to the work of Krijn [27]. The program provides a self-consistent solution of the Schrödinger, Poisson and current equations. In order to find the quantization energies the carriers are treated within the effective mass approximation and the dependence of band offsets relies on a materials database populated mostly by Vurgaftman [28]. However, more

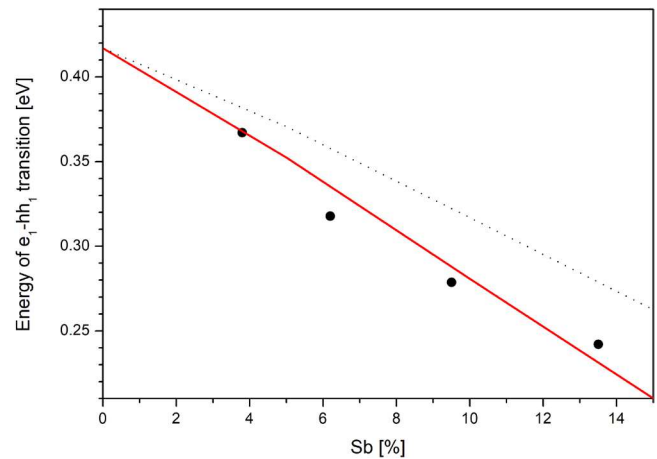


**Figure 6.** Dependence of the 4 K PL peak energies on Sb content for the InAs/InAsSb SLS structures. The best agreement with the experimental data (black circles) was obtained with an InAsSb bowing parameter of 1.63 eV split at the ratio of 40:60 between the conduction and valence bands (red line). The dotted line represents the previously highest InAsSb bowing parameter of 0.938 eV reported by Webster [29], also split at a 40:60 ratio.

recent experimental works have shown the parameters for the InAsSb alloy to be inaccurate, and therefore we made appropriate modifications. Negligible bowing of the spin orbit splitting energy was used in accordance with the work of Cripps [30]. The bowing parameters used for the non-linear interpolation of the conduction and valence band energies were  $C_{CB} = +0.65$  eV and  $C_{VB} = -0.98$  eV based on a non-zero value of  $C_{VB}$  with the bowing split between CB and VB at 40:60 ratio, as suggested by Liu [17]. The overall bowing parameter of 1.63 eV for InAsSb provides a best fit to our experimental PL results, and is larger than the highest value of 0.938 eV previously reported by Webster [29]. The agreement of the experimental 4 K PL data from figure 5 with the simulation is shown in figure 6.

Figure 7 shows for example a comparison between the MQW and SLS structures of similar Sb composition. The effect of reducing the QW separation is to raise the energy of the  $e_1$  level from 1.941 eV to 1.953 eV and similarly the energy of the  $hh_1$  level is increased from 1.579 eV to 1.583 eV. In each case the calculated transition energies are in good agreement with the PL transitions observed at 4 K.

Considering the electron and hole wavefunctions (figure 8) the heavy hole wavefunction is strongly localised within the InAsSb QW regions in both the MQW and SL structures, however in the SLS structure of thinner layers the electron wavefunction spreads out through the structure with significant probability of residing in the QW regions. Since the overlap of the electron and hole wavefunctions is directly related to the radiative recombination rate it is expected that with shorter periods the increased wavefunction overlap results in a corresponding increase in PL emission intensity. Increased anti-symmetry content increases the type II behaviour resulting in the opposite effect of reducing wavefunction overlap and is therefore detrimental to PL emission intensity.

The wavefunction overlap is proportional to the matrix element  $M$ , which can be used as a figure of merit to compare

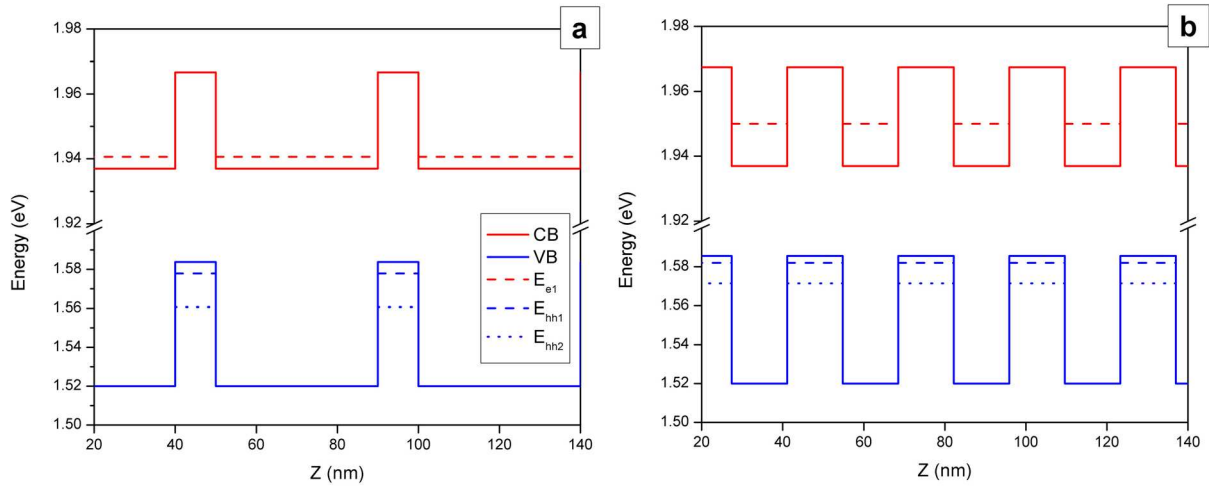


**Figure 7.** Simulated band structure (at 4K) of the MQW and SLS samples with comparable Sb content; (a) MQW (Sample 1) and (b) SLS (Sample 3). Reducing the thickness of the InAs layers raises the energy level of the eigenstates which enables convenient tuning of the emission wavelength.

different structures. As light propagates through the QW structure, photons are emitted by electrons of energy  $E_i$  in an initial state  $|i\rangle$  in the conduction band recombining with holes to a final state  $|f\rangle$  of energy  $E_f$  in the valence band.

The matrix element for this transition is defined as:

$$M = \langle f|x|i\rangle = \int \Psi_f^*(r)\Psi_i(r)d^3r \quad (5)$$

which can be separated into two terms:

$$M = M_{cv}M_{nn'} \quad (6)$$

where  $M_{cv}$  is the valence-conduction band dipole moment:

$$M_{cv} = u_c|x|u_v \quad (7)$$

and  $M_{nn'}$  is the electron-hole overlap:

$$M_{nn'} = \langle n'|hn\rangle = \int_{-\infty}^{\infty} \psi_{e_{n'}}^*(z)\psi_{h_n}(z)dz. \quad (8)$$

Since electric dipole transitions between the conduction and valence bands are strongly allowed then it can be assumed that  $M_{cv}$  is non-zero, hence the matrix element  $M$  for optical transitions is proportional to the overlap of the electron and hole states [32].

Considering the ground state transition, electrons in the  $n' = 1$  state in the conduction band recombine with holes into the  $n = 1$  state in the valence band. Furthermore, the wavefunction overlap can be considered for a single period of the periodic SL structure spanning from  $z = -\frac{P}{2}$  to  $z = +\frac{P}{2}$  containing a single QW region. Therefore, the expression for the electron-hole wavefunction overlap can be simplified:

$$M_P = \langle e|h\rangle = \int_{-P/2}^{+P/2} \psi_{e_1}^*(z)\psi_{h_1}(z)dz. \quad (9)$$

The wavefunction overlap was calculated for each structure and decreases with increasing Sb in both the MQW and SLS structures, giving a reduction of  $\sim 2.1\%$  in the SLS and a decrease of  $\sim 1.7\%$  in the MQW for a change of 1% of the antimony content in the InAsSb well in each case. The radiative recombination rate is proportional to the matrix element

squared  $M_P^2$  which was calculated for each sample and the values are given in table 2. The reduction of  $13\times$  in the experimental PL spectra of the SLS samples as the antimony content increases in the QW layers (figure 1) is more than the calculated approx.  $5.4\times$  decrease in  $M_P^2$  shown in the table. Consequently, we attribute the remaining reduction to non-radiative recombination mechanisms which are dominated by Auger processes.

The calculated ground state transition energy ( $e_1 - hh_1$ ) and the split off energy ( $E_T - \Delta_{SO}$ ) used to determine the dominant Auger process in the MQW and SLS structures as well as the corresponding activation energies are given in tables 2 and 3. In order to consider the non-radiative processes the principal Auger activation energies were determined using the transition energies and spin orbit split-off energies calculated using Nextnano. The values obtained are given in table 3 alongside the experimentally determined activation energies obtained from Arrhenius plots for each sample. Increasing the spin orbit split off energy such that it becomes larger than the band gap ( $\Delta_{SO} > E_g$ ) suppresses the CHSH process [32]. This excess is larger in the SLS samples than in the MQW samples, so CHSH Auger recombination is more suppressed in the SLS samples than in the MQW samples of similar antimony composition and CHCC dominates instead. For the SLS samples the condition given by equation (4) is satisfied for all samples except Sample 3, which has the lowest antimony content. Hence, CHCC Auger recombination is the dominant recombination process for the SLS samples and the calculated activation energy for CHCC is found to decrease with antimony content. The corresponding experimental values have uncertainties that arise due to  $CO_2$  absorption which complicates Gaussian deconvolutions at high temperatures. However, the general trend is that activation energy decreases with increasing antimony content. Note that the sample which appears to have larger activation energy with increased antimony content (Sample 6) has a thickness that exceeds the critical thickness for this structure. It is therefore reasonable to say that the overall trend of the results is consistent with the calculated CHCC Auger activation energies which dominate

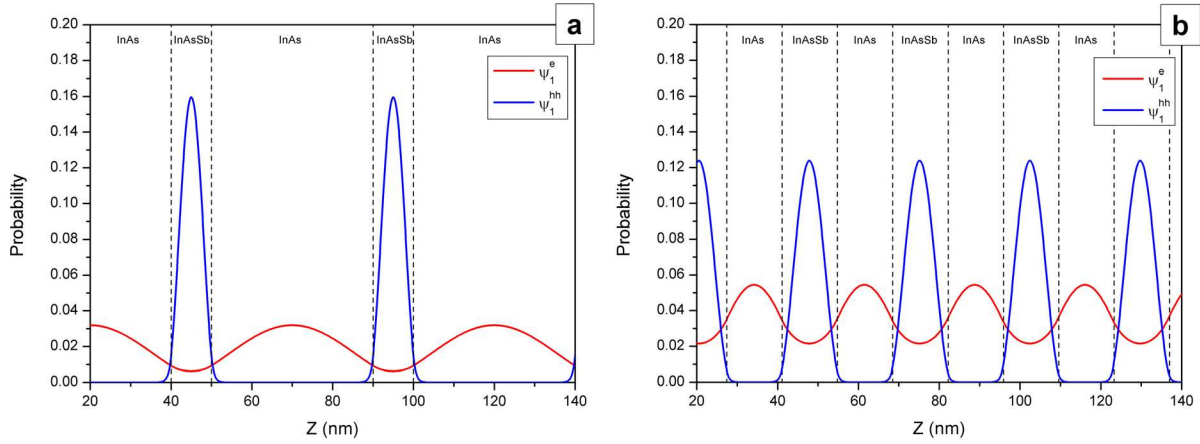


**Figure 8.** Simulation of electron (red line) and heavy hole (blue line) probabilities within structures having comparable Sb content; (a) MQW (Sample 1) and b) SLS (Sample 3). In both cases the heavy holes are strongly localised within the InAsSb QWs. The electron probability distribution inside the InAsSb QWs is significantly higher for the SLS structure, resulting in a larger overlap of the electron and heavy hole wavefunctions.

**Table 2.** Calculated and experimental values for the MQW and SLS structures at 4 K.

Sample	Sb (%)	Exp. 4 K PL peak energy (eV)	Calculated $e_1 - hh_1$ transition at 4 K (eV)	$M_p^2$	$E_T - \Delta_{SO}$ (meV)
1 (MQW)	3.7	0.376	0.377	59	39
2 (MQW)	4.3	0.367	0.369	45	54
3 (SLS)	3.8	0.367	0.369	1225	46
4 (SLS)	6.2	0.318	0.335	778	117
5 (SLS)	9.5	0.279	0.287	428	180
6 (SLS) <sup>a</sup>	13.5	0.242	0.231	228	246

<sup>a</sup> This sample exceeds the critical layer thickness limit calculated by Mathews Blakeslee model [24, 25].

**Table 3.** A comparison of the experimentally determined activation energies and the calculated values of the main Auger recombination processes. Activation energies for Auger recombination mechanisms calculated using Nextnano compared with experimentally determined values from PL.

Sample	Sb (%)	$ E_T - \Delta $ (meV)	$\frac{(E_T - \Delta)/E_T}{m_e/m_{SO}}$	$E_a^{CHCC}$ (meV)	$E_a^{CHSH}$ (meV)	$E_a$ expt. (meV)
1 (MQW)	3.7	39	0.7	20	9	33 ± 3
2 (MQW)	4.3	54	1.0	19	13	46 ± 4
3 (SLS)	3.8	46	0.9	19	11	32 ± 3
4 (SLS)	6.2	117	2.5	17	27	28 ± 4
5 (SLS)	9.5	180	4.5	15	42	22 ± 4
6 (SLS) <sup>a</sup>	13.5	246	7.1	13	58	24 ± 5

<sup>a</sup> This sample exceeds the critical layer thickness limit.

the SLS samples. Meanwhile, for the MQW samples, the calculated CHSH Auger activation energy in the higher antimony sample (Sample 2) is larger, consistent with CHSH being suppressed due to  $E_T \sim \Delta_0$  detuning, which is strongly dependent on antimony content. The experimentally determined activation energy is larger than both the calculated activation energies for the CHCC and CHSH processes, which indicates that Auger recombination is reduced in these type-II MQW structures. The experimental activation energies for the SLS samples are also significantly higher than those calculated for CHCC based on Nextnano. However, the calculated activation energies do not include Coulombic effects or band bending and more detailed calculations which account for the difference in  $e-h$  overlap and the corresponding radiative recombination are required to properly reconcile the calculated and

experimental values. Nevertheless, we observed clear differences in the temperature dependent PL spectra which show that the holes remain better confined at higher temperatures in the SLS than in the MQW. We attribute this to Coulombic attraction arising from the increased  $e-h$  overlap in the SLS because of the thinner InAs barriers between the InAsSb wells.

## Conclusion

High quality InAs/InAs<sub>1-x</sub>Sb<sub>x</sub> ( $x = 3.7-13.5$ ) type-II MQW and SLS structures on InAs substrates have been fabricated by MBE and investigated using XRD and PL spectroscopy as the basis for the active region of MIR LEDs operating at room temperature. The 4 K PL spectra of these samples exhibit the expected peak shift to longer wavelength and a

reduction in intensity as the Sb content is increased. Band structure simulations highlight the effects of changing the structure, specifically the antimony content and the layer thicknesses, to tailor the overlap of the electron and hole wavefunctions to maximise the radiative recombination rate. Analysis of the PL data along with Nextnano modelling of the structures enabled a comparison of the experimentally derived activation energies with calculated activation energies for the characteristic non-radiative Auger processes and  $e-h$  overlaps. The dominant Auger process was determined to be CHCC in the SLS structures and CHSH in the MQW structures. In the SLS structures the activation energies follow a downward trend with increasing antimony content, whereas the MQW exhibited the opposite behaviour. In both cases the experimental activation energies are larger than the calculated values, indicating some degree of Auger suppression. PL studies revealed the desired InAs to InAsSb ground state transition exists up to room temperature in the SLS structures, but not in the MQW which exhibit increasingly InAs bulk-like behaviour above  $\sim 100$  K. This is attributed to an increased  $e-h$  overlap and a larger Coulomb attraction which keeps the holes better confined in the SLS, thus preserving the transition up to high temperatures. We consider that the SLS structures are therefore an excellent prospect for room temperature LEDs.

## Acknowledgments

We gratefully acknowledge financial support for this work from EPSRC (EP/J015849/1) and for providing a studentship for J A Keen. All data created during this research are openly available from Lancaster University data archive at <https://doi.org/10.17635/lancaster/researchdata/195>.

## ORCID iDs

J A Keen  <https://orcid.org/0000-0002-7065-7871>

D Lane  <https://orcid.org/0000-0001-6647-2869>

M Kesaria  <https://orcid.org/0000-0003-1664-0806>

## References

- [1] Krier A *et al* 2004 Fundamental physics and practical realization of mid-infrared photodetectors *Proc. SPIE* **5564** 92–104
- [2] Smith D *et al* 1997 Comparison of IR LED gas sensors with thermal source products *IEE Proc., Optoelectron.* **144** 266–70
- [3] Lin C H *et al* 1997 Room-temperature low-threshold type-II quantum-well lasers at  $4.5 \mu\text{m}$  *IEEE Photonics Technol. Lett.* **9** 1573–5
- [4] Cao G 2004 *Nanostructures and Nanomaterials: Synthesis, Properties and Applications* (London: Imperial College Press)
- [5] Steenbergen E H *et al* 2012 Strain-balanced InAs/InAsSb type-II superlattices grown by molecular beam epitaxy on GaSb substrates *J. Vac. Sci. Technol. B* **30** 02B107
- [6] Lackner D *et al* 2012 InAs/InAsSb strain balanced superlattices for optical detectors: material properties and energy band simulations *J. Appl. Phys.* **111** 034507
- [7] Kurtz S R *et al* 1988 Prototype InAsSb strained-layer superlattice photovoltaic and photoconductive infrared detectors *IEEE IEDM* pp 479–82
- [8] Kurtz S R *et al* 1989 Long-wavelength InAsSb strained-layer superlattice photovoltaic infrared detectors *IEEE Electron Device Lett.* **10** 150–2
- [9] Celtek O O *et al* 2012 InAs/InAsSb type-II superlattice: a promising material for mid-wavelength and long-wavelength infrared applications *Proc. SPIE* **8353** 83533F
- [10] Klipstein P C *et al* 2014 Modelling InAs/GaSb and InAs/InAsSb superlattice infrared detectors *J. Electron. Mater.* **43** 2984–90
- [11] Zhang Y H, Miles R H and Chow D H 1995 InAs-InAsSb type II superlattice midwave infrared lasers grown on InAs substrates *IEEE J. Sel. Top. Quantum Electron.* **1** 749–56
- [12] Wilk A *et al* 2000 Type-II InAsSb/InAs strained quantum-well laser diodes emitting at  $3.5 \mu\text{m}$  *Appl. Phys. Lett.* **77** 2298
- [13] Christol P *et al* 2000 InAs/InAs(P,Sb) quantum-well laser structure for the midwavelength infrared region *IEE Proc., Optoelectron.* **147** 181–7
- [14] Biefeld R M *et al* 1998 Recent advances in mid-infrared ( $3-6 \mu\text{m}$ ) emitters *Mater. Sci. Eng. B* **51** 1–8
- [15] Hardaway H R *et al* 1999 Optical studies of InAs/In(As,Sb) single quantum well (SQW) and strained-layer superlattice (SLS) LEDs for the mid-infrared (MIR) region *Proc. SPIE* **3621** 124–33
- [16] Golovin A S *et al* 2010 LEDs based on InAs/InAsSb heterostructures for CO<sub>2</sub> spectroscopy ( $4.3 \mu\text{m}$ ) *Technol. Phys. Lett.* **36** 47–9
- [17] Liu P W *et al* 2006 Photoluminescence and bowing parameters of InAsSb/InAs multiple quantum wells grown by molecular beam epitaxy *Appl. Phys. Lett.* **89** 201115
- [18] Miller D A B 1996 Quantum dynamics of simple systems *Quantum Semiclass. Opt.* **8**
- [19] Bugajski M and Reginski K 1996 Optical properties of semiconductor quantum wells *Optoelectron. Rev.* **4** 83–100
- [20] Ridley B K 1993 *Quantum Processes in Semiconductors* (Oxford: Clarendon)
- [21] Lock D 2005 Investigations into the high power limitations of semiconductor laser diodes *PhD Thesis* University of Surrey
- [22] Choi H K 2004 *Long Wavelength Infrared Semiconductor Lasers* (New York: Wiley)
- [23] Varshni Y P 1967 Temperature dependence of the energy gap in semiconductors *Physica* **34** 149–54
- [24] Matthews J E and Blakeslee A E 1974 Defects in epitaxial multilayers *J. Cryst. Growth* **27** 118–25
- [25] Lackner D 2011 InAsSb/InAs strain balanced superlattices for photodetector applications *PhD Thesis* Simon Fraser University
- [26] Birner S *et al* 2007 Nextnano: general purpose 3D simulations *IEEE Trans. Electron Devices* **54** 2137
- [27] Krijn M P C N 1991 Heterojunction band offsets and effective masses in III–V quaternary alloys *Semicond. Sci. Technol.* **6** 27–31
- [28] Vurgaftman I, Meyer J R and Ram-Mohan I R 2001 Band parameters for III-V compound semiconductors and their alloys *J. Appl. Phys.* **89** 5815
- [29] Webster P T *et al* 2015 Measurement of InAsSb bandgap energy and InAs/InAsSb band edge positions using spectroscopic ellipsometry and photoluminescence spectroscopy *J. Appl. Phys.* **118** 245706
- [30] Cripps S A *et al* 2007 Midinfrared photorefectance study of InAs-rich InAsSb and GaInAsPSb indicating negligible bowing for the spin orbit splitting energy *Appl. Phys. Lett.* **90** 172106
- [31] Svensson S P *et al* 2017 Materials design parameters for infrared device applications based on III-V semiconductors *Appl. Opt.* **56** B58–63
- [32] Singh J and Williams R T 2014 *Exciton and Photonic Processes in Materials* (Berlin: Springer)